Development of Software for the Interpretation of Radar Images using Deep Learning Methods

Kazizat Iskakov, Almaz Tatin

L. N. Gumilyov Eurasian National University, 11 Pushkin street, 010005 Astana, Kazakhstan; 550220300753@enu.kz; 980111350924@enu.kz

Abstract: This study introduces a practical method for diagnosing subsurface structures which focuses on roads and uses ground-penetrating radar (GPR) and deep learning. The study proposes an implementation to interpret radargrams captured by the OKO-2 system, which records signals reflected from underground layers. Two interpretation methods are used, i.e., one based on physics formulas, the other on mathematical modeling. Before applying neural networks, the data undergo analytical processing using the GeoScan32 software, which filters noise, enhances signals, and identifies layer boundaries. This analytical foundation is crucial for effectively training deep learning models to interpret complex subsurface data.

Keywords: Geophysics; software; ground penetrating radar; geoelectric section; Fourier transform; Hilbert transform; ill-posed and inverse problems

1 Introduction

Application of non-destructive electromagnetic surveying methods to investigate heterogeneous media enforces a significant challenge in the interpretation of radargrams. The primary method to study the subsurface structures is ground-penetrating radar (GPR). Typically, GPR provides data on signal travel times through heterogeneous media. From a mathematical perspective, these travel times correspond to a time-dependent function that represents wave propagation [1]. The main task in radargram interpretation is to reconstruct functions dependent on depth from the time-domain data, characterizing the properties of the heterogeneous medium. This problem belongs to the class of ill-posed inverse problems. Developing algorithms and software to address this class of problems is of significant relevance and practical importance, particularly in applications such as archaeological site detection and the monitoring of road surfaces, highways, and airstrips. The GPR has undergone significant advancements over the past three decades. It covers various aspects of geophysical science, technology, and scientific and engineering applications [2]. Georadar systems play a crucial role in

non-destructive testing and diagnostics within the construction industry, such as in the inspection of buildings, road surfaces (e.g., aerodromes), and mineral exploration. These systems emit electromagnetic signals into the survey environment, capture reflected signals, and generate radargrams based on these reflections. Radargrams represent time-domain scans at observation points. The main goal of experimental studies is to interpret these radargrams. Engineers and researchers accomplish this by comparing obtained radargrams with reference patterns in databases and performing additional calculations based on wave propagation theory. Practical and theoretical methods related to subsurface radar are documented in works by local and international authors [3]-[4]. Inverse problems related to hyperbolic equations arise in various practical contexts, including seismology, georadar technology, medicine, and electric network theory [5]-[9]. For numerical methods concerning coefficient-based hyperbolic inverse problems, readers are referred to the monograps [10]-[11]. Additionally, methods have been developed for solving direct radar problems in horizontally layered media. The layer-by-layer recalculation method was used in [12]-[13], and further algorithms were proposed in [14]-[15]. In recent years, train-mounted GPR has become a widely used tool for fast and non-destructive assessment of railway infrastructure prior to track rehabilitation works on the French railway network. Accurate evaluation of the substructure condition is crucial, as it directly affects the planning and quality of maintenance operations. However, the interpretation of GPR data remains a complex and time-consuming process that typically requires expert involvement. Kahil et al. [16] proposed two methods to improve and automate GPR data analysis for railway diagnostics. The first uses entropy-based signal processing to measure layer thickness, detect fouling, and locate water retention, with field tests confirming its accuracy. The second applies deep learning to identify mud pumping defects, a common railway issue, with strong results for severe cases. These approaches support the development of more automated diagnostic tools and inform the current study.

2 Experimental Investigations of the Highway

We assess the condition of road pavement along the Astana–Makinka highway using a mobile diagnostic lab equipped with Oko-2 ground-penetrating radar. The lab uses two antenna types: 400 MHz for deeper scans up to 3 meters and 1000 MHz for higher-resolution images of shallow layers. The experiment highlights the use of the 1000 MHz antenna to analyze the area between asphalt and crushed stone. Signal cleaning, including denoising and interference removal, was carried out using GeoScan32 software on data collected from this antenna.

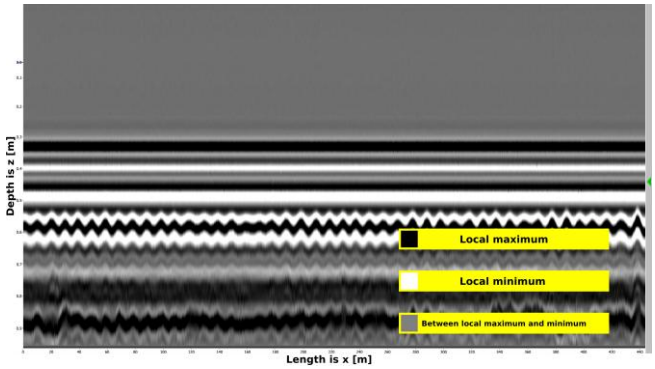

Figure 1
Signal Data over 500 Meters

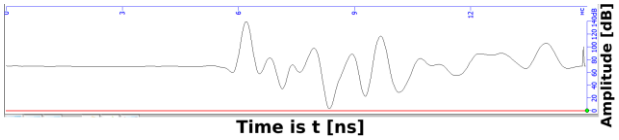

Figure 2
Signal Data at a Specific Point of the Profile

The white and black horizontal lines show the signal's peaks and valleys, while gray lines mark transitions between them. A vertical slice through the profile reveals a 2D signal graph called a trace, and many traces together form the full radar image. Traces are taken every 15 centimeters. As a first processing step, the signal gain is initially set to zero.

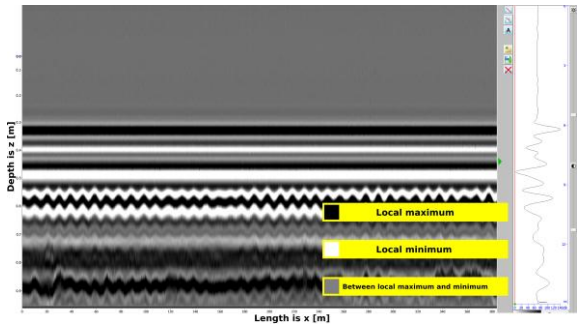

Figure 3
Signal Data with Zero Gain

In the second step, band-pass filtering is applied to remove industrial noise from the signal, including interference from cables, wires, and vehicle sounds, yielding the trace presented in Figure 4.

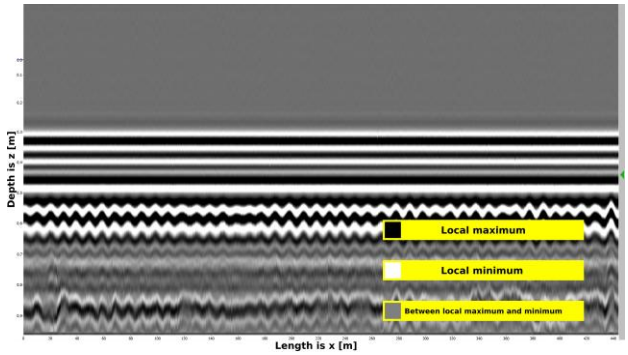

Figure 4
Signal Data after Industrial Noise Removal

In the third step, mean subtraction is applied, in which the mean across all traces is computed and subtracted from each trace. Next, automatic gain control is applied to enhance the visibility of layer boundaries within the road structure. The processed signal data after mean subtraction and automatic gain control are presented in Figure 5. In the final step, the layers of the road pavement are delineated.

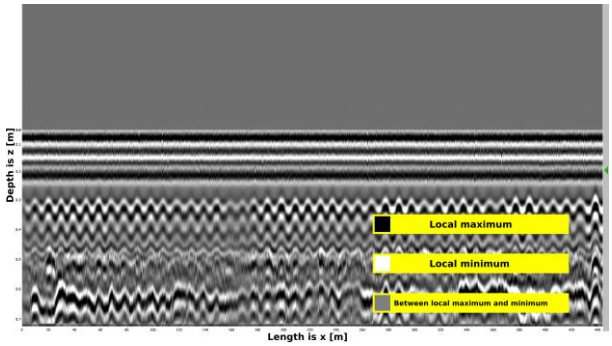

Figure 5
Signal Data after Automatic Gain Control

Figure 6 uses color to show different road layers: white for air, yellow for asphalt, and brown for crushed stone. By GeoScan32 and layer thicknesses, we calculate each layer's dielectric permittivity, as in Figure 7, the asphalt layer (yellow) is 300 mm thick with a permittivity of 4.38. To analyze deeper layers like the crushed stone, a lower-frequency antenna, e.g., 400 MHz is needed.

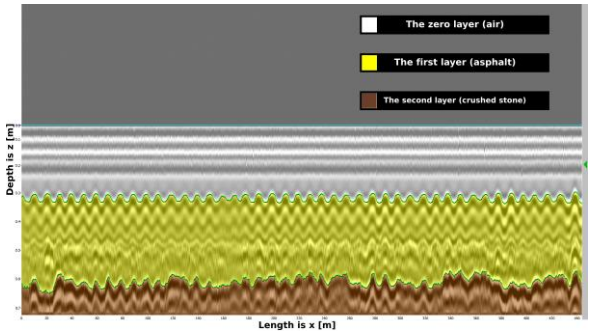

Figure 6
Signal Data after Layer Delineation

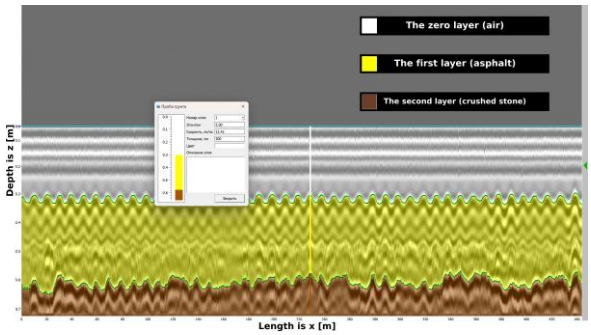

Figure 7
Determination of relative dielectric permittivity values of the signal layers

3 Hilbert Transform for GPR Signal Processing

The Hilbert transform enhances the analysis of GPR signals. We shift the signal's phase, the transform reveals energy distribution, to identify subsurface features. Applied to radar scans of road pavements, it highlights boundaries where reflections occur and improves the visibility of buried objects, especially in complex environments with inclusions or varying terrain. The transform's ability to detect energy peaks makes it valuable for outlining layer geometry and identifying curved reflections, such as those caused by buried objects or voids. The Hilbert transform of a function $u(t)$ is given by the following convolution:

$$H[u](t) = \frac{1}{\pi} \int_{-\infty}^{\infty} \frac{u(\tau)}{t-\tau}\, d\tau \tag{1}$$

Here, the integral is understood in the sense of the principal value . The polarity of the reflected wave pulse is determined by the values of the imaginary part of the transform at the time of the modulus maximum. A sign change indicates reflection from a medium with a lower wave velocity compared to the original medium. Conversely, if the sign remains unchanged, it signifies partial reflection and transmission into a medium with higher wave velocity. Figure 5 illustrates a typical wave field pattern and the Hilbert transform for a four-layer medium where the wave velocity reaches a minimum in the last layer. The transformation was performed using discrete equations based on the relationship between the Fourier transform and the Hilbert transform:

$$S(n) = \frac{1}{N}\sum_{k=0}^{N-1} E(k\,\Delta t)\cdot \exp(-2\pi i k n/N), \quad n = 0,1,\dots,N/2. \tag{2}$$

$$H(k\Delta tn) = 2\cdot \sum_{n=1}^{N/2} S(n)\cdot \exp(2\pi i k n/N), \quad k = 0,1,\dots,N. \tag{3}$$

4 Wavelet Filtering of GPR Signals

To remove noise from GPR signals, the Daubechies wavelet of order 4 (db4) was applied [20]. Daubechies wavelets do not have an analytical expression and are defined solely by their associated filter coefficients. In practical applications, only the approximating h_k and detail g_k coefficients are used, without computing the explicit shape of the wavelet function [21]. For the db4 wavelet, these coefficients are as follows:

$$\begin{aligned} h_0 &= 0.482962913144534, & g_0 &= h_3.\\ h_1 &= 0.8365163037378079, & g_1 &= -h_2.\\ h_2 &= 0.2241438680420134, & g_2 &= h_1.\\ h_3 &= -0.1294095225512604, & g_3 &= -h_0. \end{aligned} ,$$

The decomposition into approximation and detail components using discrete Daubechies wavelets is performed according to the following equations (4):

$$\begin{aligned} a_i &= h_0 s_{2i-1} + h_1 s_{2i} + h_2 s_{2i+1} + h_3 s_{2i+2}, \quad i = 1,2,\dots,n/2-1.\\ d_i &= g_0 s_{2i-1} + g_1 s_{2i} + g_2 s_{2i+1} + g_3 s_{2i+2}, \quad i = 1,2,\dots,n/2-1.\\ a_{n/2} &= h_0 s_{n-2} + h_1 s_{n-1} + h_2 s_0 + h_3 s_1.\\ d_{n/2} &= g_0 s_{n-2} + g_1 s_{n-1} + g_2 s_0 + g_3 s_1. \end{aligned} \tag{4}$$

The wavelet analysis cleans up signals by separating useful information from noise. It uses filters to split a signal into low and high-frequency parts. The low frequencies hold the main signal, while high frequencies often contain noise. To reduce that noise, a method called thresholding is applied to the high-frequency data. This approach is flexible and can be adjusted based on the type of signal. For best results, you need to understand the noise pattern, choose the right thresholding method, and set the right threshold level. There are two widely accepted rules for threshold clipping of wavelet coefficients:

1. Hard thresholding:

$$d_i = \begin{cases} 0, & |d_i| \le \nu, \\ d_i, & |d_i| > \nu. \end{cases}$$

2. Soft thresholding:

$$d_i = \begin{cases} 0, & |d_i| \le \nu, \\ sign(d_i)(|d_i| - \nu), & |d_i| > \nu. \end{cases}$$

Here, ν denotes the threshold value. The effectiveness of noise reduction depends on choosing the right threshold level and too low keeps noise, too high removes important details. Wavelet improves GPR signal clarity by breaking it into parts through several levels. Usually, five levels are enough to enhance resolution without losing signal quality. At each level, a threshold is applied to remove noise. The signal is then rebuilt using the main structure from the final level and cleaned details from earlier ones, step-by-step from coarse to fine. The goal is to find a threshold that improves signal quality (SNR) without distorting it. The SURE method is often used to find this optimal balance. This assumes that the detail coefficients from previous levels have been stored.

$$\nu = \delta\sqrt{2\ln n}, \text{ where } \delta = median(|d_i|)/0.6475. \quad (5)$$

$$a_1 = h_2 s_{\frac{n}{2}} + h_1 s_n + h_0 s_1 + h_3 s_{\frac{n}{2}-1}.$$

$$a_2 = g_0 s_{\frac{n}{2}} + g_1 s_{\frac{n}{2}-1} + g_2 s_1 + g_3 s_n. \quad (6)$$

$$a_i = h_2 s_{\frac{i-1}{2}} + h_1 s_{\frac{i-1}{2}+\frac{n}{2}} + h_0 s_{\frac{i-1}{2}+1} + h_3 s_{\frac{i-1}{2}+\frac{n}{2}-1},\ i = 3,5,\dots,n/2-1 \text{ (odd)}.$$

$$a_i = g_0 s_{\frac{i-1}{2}} + g_1 s_{\frac{i-1}{2}+\frac{n}{2}-1} + g_2 s_{\frac{i-1}{2}+1} + g_3 s_{\frac{i-1}{2}+\frac{n}{2}}\ i = 4,6,\dots,n/2 \text{ (even)}.$$

5 Inverse Problem in the Frequency Domain

The physical formulation of the subsurface radar imaging problem is presented below. Data acquisition is performed on the surface of a road pavement using the OKO-2 automotive georadar system, equipped with 400 MHz and 1000 MHz

antennas. Different layers of the road structure exhibit distinct values of dielectric permittivity and electrical conductivity. An electromagnetic pulse is transmitted into the subsurface by the GPR transmitter and antenna, and the receiving antenna captures the medium's response, which consists of waves varying in travel time, amplitude, and waveform. The inverse problem in subsurface radar imaging involves reconstructing the underground medium's structure using GPR data representing the medium's response. We now examine the problem formulation, which has been thoroughly studied with respect to the uniqueness of solutions for both the direct and inverse geoelectric equations in works [10]. Consider an external current source of the form:

$$\begin{pmatrix}0\\1\\0\end{pmatrix} g(x)\,\delta(z-z_*)\theta(t)\,f(t) \tag{7}$$

The excitation of an external current, as represented by equation (7), corresponds to the instantaneous switching of a current parallel to the axis *Oy* and localized at the point z_*. This current is distributed along the axis *Ox* with a density $g(x)$, e.g., representing an infinitely long cable. Over time, the current behavior is described by a function $f(t)$. Now, let's consider a N_l-layered structure with boundaries at z_k ($k = \overline{0, N_l}$) and $z_0 = 0$; the m-th layer spans the interval $[z_{m-1}, z_m]$, and the last (subbase) layer extends into half-space $[z_{N_l}, \infty)$, while the air occupies half-space $(-\infty, 0]$ (see Figure 8).

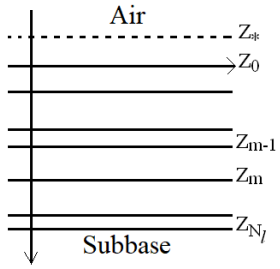

Figure 8
The medium model is horizontally layered

The electromagnetic properties of each layer are characterized by the values of dielectric permittivity $\varepsilon_0\varepsilon$, conductivity σ, and magnetic permeability $\mu_0\mu$. The known values are $\varepsilon_0 = 8.854 \cdot 10^{-12}$ F/m and $\mu_0 = 4\pi \cdot 10^{-7}$ H/m. For a sufficiently wide range of materials, the value of ε varies within the interval [1,80], while μ remains constant at 1. Therefore, magnetic permeability is considered a known constant. Since the medium is horizontally layered, the parameters ε, σ are piecewise constant functions of the variable z ($z \in (-\infty, \infty)$). It is assumed that, at the initial time, the electromagnetic field is in a state of rest:

$$E|_{t<0} \equiv 0, \quad H|_{t<0} \equiv 0. \tag{8}$$

Under the aforementioned physically justified assumptions, the system of Maxwell's equations is reduced to three equations [10], which can be further simplified to a single equation. By then applying the Fourier transform with respect to the horizontal variable x and the time variable t:

$$u(\omega,\lambda,z)=\int_{-\infty}^{\infty}\int_{-\infty}^{\infty}E_2(t,x,z)e^{i(\omega t+\lambda x)}\,dxdt.$$

This leads to the following problem formulation [24]:

$$u_{zz}-(\lambda^2-\omega^2\mu_0\varepsilon_0\varepsilon+i\omega\mu_0\sigma)u=0, \tag{9}$$

$$[u]_{z_j}=0,\quad [u_z]_{z_j}=0,\quad j=\overline{0,N_1},\quad [u]_{z_*}=0,\quad [u_z]_{z_*}=-f(\omega)\mu_0. \tag{10}$$

Here, λ and ω are the parameters of the Fourier transform with respect to the variables x and t, respectively. The notation $[\cdot]$ is used for conjugation, that is, $[w]_z=w(z+0)-w(z-0)$.

The following notation is introduced:

$$k^2=\lambda^2-\chi,\quad \chi=\omega^2\mu_0\varepsilon_0\varepsilon+i\omega\mu_0\sigma. \tag{11}$$

The function k is piecewise constant, as both ε and σ are piecewise constant functions. The most significant influence on the change in k comes from variations in ε and σ, especially when $\omega^2\mu_0\varepsilon_0\varepsilon\approx\omega\mu_0\sigma$ and $\lambda^2\sim\omega^2\mu_0\varepsilon_0\varepsilon$.

Assuming $\omega^2\mu_0\varepsilon_0\varepsilon=\omega\mu_0\sigma$, the following result is obtained:

$$\omega_0=\frac{\sigma}{\varepsilon_0\varepsilon} \tag{12}$$

The decay conditions at infinity are given by:

$$u\to 0\ \ (x\to\pm\infty) \tag{13}$$

Assume additional information (the medium's response) is known with respect to the solution of the direct problem (9)–(11):

$$u|_{z=0}=g(\omega,\lambda). \tag{14}$$

To find solutions for the direct problem (9)-(11), the original equation is transformed into a Riccati equation, and the layer-by-layer recalculation method [20] is applied.

After applying the layer-by-layer recalculation method, the solution to the forward problem (9)–(11) is obtained over the interval $[z_*,0]$ and within each interval $[z_{m-1},z_m]$

$$u|_{z=0}\equiv u^0=u^*\frac{2k_0e^{-2k_0z_*}}{(s^0+k_0)e^{-2k_0z_*}-(s^0-k_0)}.$$

$$u(z) = u^{m-1}e^{k_m(z_{m-1}-z)}\frac{(s^m + k_m)e^{2k_m(z-z_m)} + (s^m - k_m)}{(s^m + k_m)e^{-2k_m(z_m-z_{m-1})} - (s^m - k_m)}. \quad (15)$$

The values of u^*, s^0, u^0, u^{m-1} and s^m are calculated using the recursive formulas presented in studies [24].

6 Neural Networks Modeling

Several machine learning models had previously addressed modeling of pavement, e.g., [25-30]. We aim at using Neural Networks. Assume that additional information (the medium's response) is known with respect to the solution of the direct problem (9)-(11). From equation (9), using the known expressions (10)-(11) and the additional information (11), the objective is to reconstruct the set of parameters:

$$\Theta = (\varepsilon_*, \varepsilon_1, \varepsilon_2, \varepsilon_3, \varepsilon_4) \quad (16)$$

$$\Sigma = (\sigma_*, \sigma_1, \sigma_2, \sigma_3, \sigma_4) \quad (17)$$

Here, the sets ε_i, σ_i represent the dielectric permittivity and specific conductivity of the i-th layer, while the pair ε_*, σ_* corresponds to the dielectric permittivity and specific conductivity of air, with $\varepsilon_* = 1$ and $\sigma_* = 0$. To find the parameter sets (16)-(17), the process begins with constructing computational groups for all possible parameter combinations, as described below:

$$P^{(m)} = \left(p_0^{(m)}, p_1^{(m)}, p_2^{(m)}, p_3^{(m)}, p_4^{(m)}\right), \quad m = \overline{1, N_p}, \quad (18)$$

$$Q^{(n)} = \left(q_0^{(n)}, q_1^{(n)}, q_2^{(n)}, q_3^{(n)}, q_4^{(n)}\right), \quad n = \overline{1, N_q}, \quad (19)$$

$$P = \left\{P^{(m)} \mid m = \overline{1, N_p}\right\}, \quad Q = \left\{Q^{(n)} \mid n = \overline{1, N_q}\right\}. \quad (20)$$

Here, group P corresponds to dielectric permittivity ε, and group Q corresponds to specific conductivity σ. Constructing these groups (18)-(20) is feasible since dielectric permittivity ε varies from 1 to 80 in the medium, and specific conductivity σ ranges from 0 to 1. The obtained groups P and Q are combined into a unified group PQ, which takes the following form:

$$PQ^{(m,n)} = \left(P^{(m)}, Q^{(n)}\right), \quad m = \overline{1, N_p}, \quad n = \overline{1, N_q}, \quad (21)$$

$$PQ = P \times Q = \left\{PQ^{(m,n)} \mid m = \overline{1, N_p}, \quad n = \overline{1, N_q}\right\}. \quad (22)$$

Piecewise constant functions $p^{(m)}(z)$ and $q^{(n)}(z)$ are introduced for groups P and Q, respectively:

$$p^{(m)}(z) = \begin{cases} p_0^{(m)}, & z \in (-\infty, 0], \\ p_1^{(m)}, & z \in [0, z_1], \\ p_2^{(m)}, & z \in [z_1, z_2], \\ p_3^{(m)}, & z \in [z_2, z_3], \\ p_4^{(m)}, & z \in [z_3, \infty), \end{cases} \quad m = \overline{1, N_p}, \tag{23}$$

$$q^{(n)}(z) = \begin{cases} q_0^{(n)}, & z \in (-\infty, 0], \\ q_1^{(n)}, & z \in [0, z_1], \\ q_2^{(n)}, & z \in [z_1, z_2], \\ q_3^{(n)}, & z \in [z_2, z_3], \\ q_4^{(n)}, & z \in [z_3, \infty), \end{cases} \quad n = \overline{1, N_q}. \tag{24}$$

Here, functions $p^{(m)}(z)$ and $q^{(n)}(z)$ correspond to parameter sets $P^{(m)}$ and $Q^{(n)}$.

Subsequently, for each parameter set $PQ^{(m,n)}$ from the overall PQ group, the direct problem is solved:

$$u_{zz}^{(m,n)} - \left(k^{(m,n)}\right)^2 u^{(m,n)} = 0, \quad m = \overline{1, N_p}, \quad n = \overline{1, N_q} \tag{25}$$

$$\left[u^{(m,n)}\right]_{z_j} = 0, \ \left[u_z^{(m,n)}\right]_{z_j} = 0, \ \left[u^{(m,n)}\right]_{z_*} = 0, \ \left[u_z^{(m,n)}\right]_{z_*} = -f(\omega)\mu_0. \tag{26}$$

The coefficient $k^{(m,n)}$ is chosen such that:

$$k^{(m,n)} = \left(\lambda^{(m,n)}\right)^2 - \left(\omega^{(m,n)}\right)^2 \mu_0 \varepsilon_0 p^{(m)} + i\omega^{(m,n)} \mu_0 q^{(n)},$$

where $p^{(m)}$ and $q^{(n)}$ represent the piecewise constant functions (23) and (24), respectively. The solutions obtained from (25)-(26) are combined into a solution group U:

$$U = \left\{u^{(m,n)} \mid m = \overline{1, N_p}, \quad n = \overline{1, N_q}\right\}. \tag{27}$$

Due to the uniqueness theorem, for the direct problems (25)–(26), each parameter set $PQ^{(m,n)}$ from group PQ corresponds to a unique solution $u^{(m,n)}$ from group U, and vice versa. Furthermore, due to the same uniqueness theorem, applying a neural network allows us to precisely determine the solution (25)-(26) for the inverse problem. Consider a quadratic functional of the following form:

$$J = J[p, q] = \int_{\omega_0 / C}^{C\omega_0} \left[u(\omega, \lambda_0, 0; \varepsilon, \sigma) - u\left(\omega, \lambda_p, 0; p, q\right)\right]^2 d\omega \tag{28}$$

where $\lambda_0^2 = \omega_0^2 \mu_0 \varepsilon_0 \varepsilon$, $\lambda_p^2 = \omega_0^2 \mu_0 \varepsilon_0 p$ and p, q are the parameters of the solution $u(\omega, \lambda_0, 0; p, q)$ from equations (9)-(11), replacing ε, σ with p, q, respectively. The task is to minimize the quadratic functional and find approximate values of

p, q that approximate the exact values of ε, σ, respectively. For this purpose, we construct an iterative process (similar to the gradient descent method):

$$p^{(r+1)} = p^{(r)} - \alpha^{(r)} \cdot \nabla J\left[p^{(r)}, q^{(r)}\right], \qquad r = 0,1,2,\ldots \tag{29}$$

$$q^{(r+1)} = q^{(r)} - \beta^{(r)} \cdot \nabla J\left[p^{(r)}, q^{(r)}\right], \qquad r = 0,1,2,\ldots \tag{30}$$

Although, from an optimization perspective, the functional is a constant and its gradient is zero, from the neural network's viewpoint, the functional depends on parameters p, q, and the gradients of the functional are non-zero. Thus, the iterative processes (29)-(30) are meaningful in terms of existence. The sequence of approximations (29)–(30) is rewritten as follows:

$$p^{(r+1)} = p^{(r)} - \alpha^{(r)} \cdot \nabla_p J\left[p^{(r)}, q^{(r)}\right], \qquad r = 0,1,2,\ldots \tag{31}$$

$$q^{(r+1)} = q^{(r)} - \beta^{(r)} \cdot \nabla_q J\left[p^{(r)}, q^{(r)}\right], \qquad r = 0,1,2,\ldots \tag{32}$$

The idea is to train the neural network to find an approximate solution $p^{(r_*)}, q^{(r_*)}$ that corresponds to the accurate solutions ε, σ from the overall PQ parameter group.

7 Numerical Analysis

The Hilbert transform is calculated using the signal's discrete Fourier transform, which avoids complex integral calculations. It was applied to radar data from layered road and subsurface structures. In the example shown, markers indicate layer boundaries, with the first marking the ground surface. The original signal is shown in orange, and its Hilbert transform in violet.

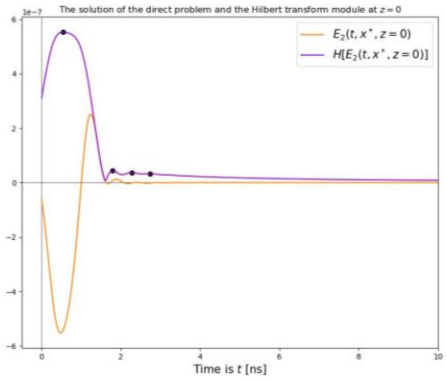

Figure 9

Hilbert transform of a road pavement radargram for a four-layer medium with velocity minimum

Examples are presented of transformations performed for media with irregular subbase surfaces. In the case of distinct subsurface relief, such as a single depression illustrated in Figure 9, the line of maxima in the transformation exhibits distortion within the relief depressions and closely follows the shape of the relief depression, as illustrated in Figure 11. Additionally, the layer boundaries, represented by the 2nd, 3rd, and 4th horizontal lines in Figure 11, are distinctly identifiable. The performance is validated through a comparison of the results with transformations provided by the NumPy package in Python. GPR often lack clear guidance for interpreting data. A custom software was developed to test new filtering and visualization methods, including wavelet-based processing and Fourier analysis of signals. This tool helps users clean and visualize GPR data more accurately, improving interpretation beyond what typical commercial software offers.

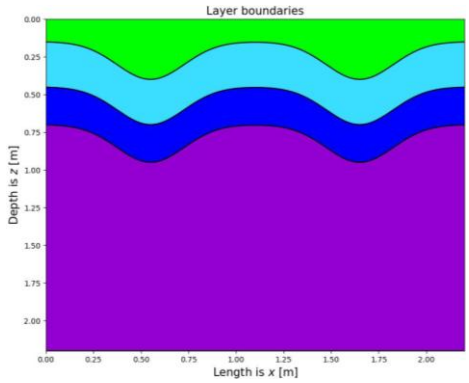

Figure 10
Model of a medium with relief layered subbase

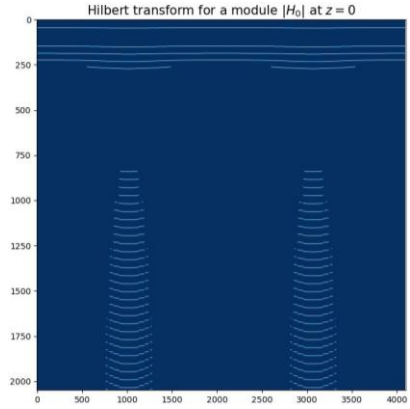

Figure 11
Hilbert transform for a model medium with relief four-layer subbase

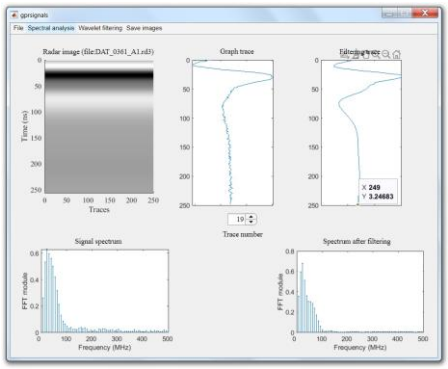

Figure 12
Software Interface Window

7.3 Numerical Solution of the Direct Problem in Frequency Domain

Let us consider a model of the medium corresponding to road pavement: The first layer consists of fine-grained and coarse-grained asphalt, along with a fiberglass mesh layer. The second layer is a base layer composed of a mixture of fine gravel with a particle size of 0.4 mm and containing 7% cement by weight. The third layer is a base layer composed of a mixture of coarse gravel with a particle size of 0.8 mm. The fourth layer consists of the subbase, which is clay-rich soil.

Table 1
Represents the road structure model

layer number	A	B	C	Subbase
ε (relative)	3.0	6.0	4.0	20.0
σ [S/m]	0.00512	0.00725	0.00592	0.0132
z_k [m]	0.15	0.45	0.70	2.20

Since the functions $\varepsilon(z)$ and $\sigma(z)$ are piecewise constant, it is straightforward to compute their average values using depth-averaged integrals:

$$\varepsilon_{mean} = \frac{1}{h}\int_0^h \varepsilon(z)\, dz \approx 15.1, \qquad \sigma_{mean} = \frac{1}{h}\int_0^h \sigma(z)\, dz \approx 0.0115\ [\mathrm{S/m}].$$

The characteristic circular frequency $\omega_0 \approx 8.6 \cdot 10^7$ is calculated using formula (9). Figure 13 shows the external current source $f(t)$ with a duration of 1.5 ns:

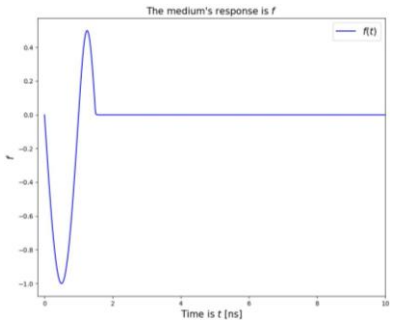

Figure 13
External Current Source

Figures 14 and 15 depict $\mathbf{Re}\{u(\omega,\lambda,0)\}$ and $\mathbf{Im}\{u(\omega,\lambda,0)\}$, respectively, for the selected road structure model:

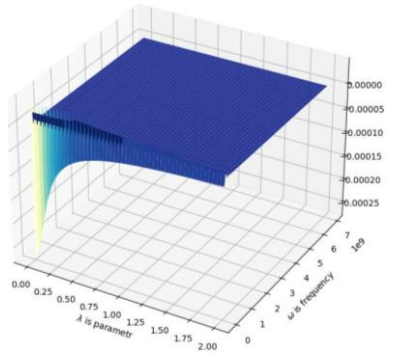

Figure 14
$\mathbf{Im}\{u(\omega,\lambda,0)\}$

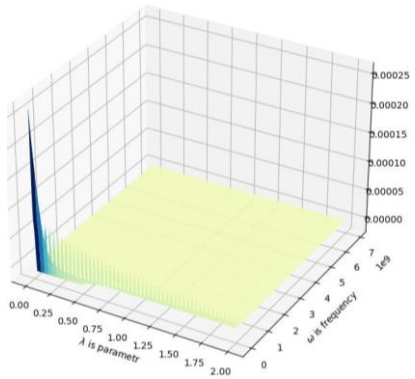

Figure 15
$\mathbf{Re}\{u(\omega,\lambda,0)\}$

The circular frequency varies in the interval $[\omega_0/80, 80\omega_0]$ with $N_\omega = 4096$. Since $\omega_0\mu_0\sigma \approx 1.11$, the spatial frequency is chosen from the interval [0, 2] with $N_\lambda = 4096$.

8 Results of Applying Neural Networks for Inverse Problems in Subsurface Radar Imaging

Based on the available supplementary data, the subsurface medium structure was successfully reconstructed using a neural network. Table 2 below provides the dielectric permittivities and specific conductivities of the actual subsurface medium, as well as their corresponding approximate values.

Table 2
Exact and approximate characteristics of the given medium

layer number	1	2	3	subbase
ε (relative)	3.0	6.0	4.0	20.0
σ [S/m]	0.00512	0.00725	0.00592	0.0132
p	3.11	5.92	4.21	20.32
q [S/m]	0.00521	0.0072	0.00607	0.0133

Here, ε, σ represent the exact medium characteristics, and p, q corresponds to their approximate values, respectively.

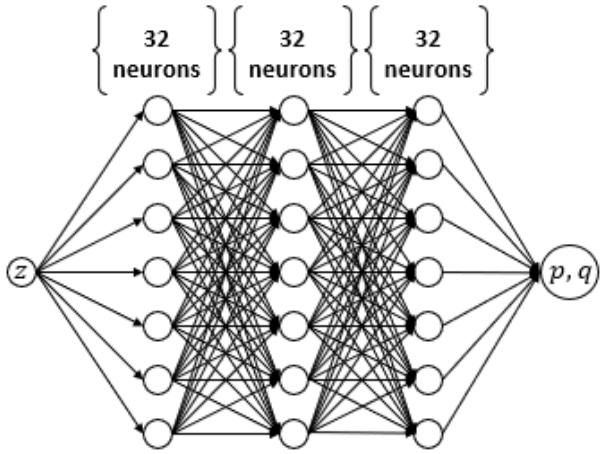

Figure 16
Neural Network Architecture

Figure 16 illustrates the architecture of a neural network designed to approximate the medium characteristics p and q. A three-layer neural network, with 32 neurons in each layer, was used. The network accepts a single spatial variable z (depth) as input and outputs a parameter p (or q), corresponding to the dielectric permittivity (or specific conductivity). The hyperbolic tangent function was selected as the activation function. The Adam optimization method, with a learning rate of 10^{-4}, was employed for training. This step was determined experimentally and demonstrated the best convergence of the parameters p and q. It is important to consider that parameter p, which corresponds to the relative permittivity ε, varies within the range [1, 80], while parameter q, representing the electrical conductivity σ, ranges from 0 to 1. Since the hyperbolic tangent function outputs values in the interval [-1, 1], it is necessary to scale this output to match the target intervals [1, 80] and [0, 1], corresponding to ε and σ, respectively. Therefore, a data validation process is performed at each iteration of the training procedure. The quadratic functional (28) was used as the loss function.

The exact and approximate solutions to the direct problem, along with the relative error, are presented in Figures 17 and 18. Additionally, the L_2 norm error is of the following order:

$$\left\| E_2(t, x_*, 0) - \hat{E}_2(t, x_*, 0) \right\|_{L_2} = 5.6 \cdot 10^{-11}$$

The approximate solution in Figure 17 was derived using the neural network algorithm for solving the inverse problem. The approximate solution presented in Figure 17 was obtained by applying an intelligent method for solving the inverse problem. Figures 17 and 18 compare the exact and approximate values of the additional information — specifically, the medium's response. It is important to note that the most significant changes occur within the time range of 1.5 ns to 2.5 ns. This behavior can be attributed to variations in the values of relative permittivity ε and electrical conductivity σ , which depend on the properties of the surrounding medium.

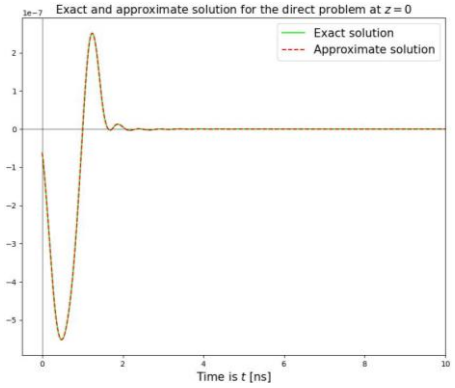

Figure 17
Exact and approximate solutions to the direct problem

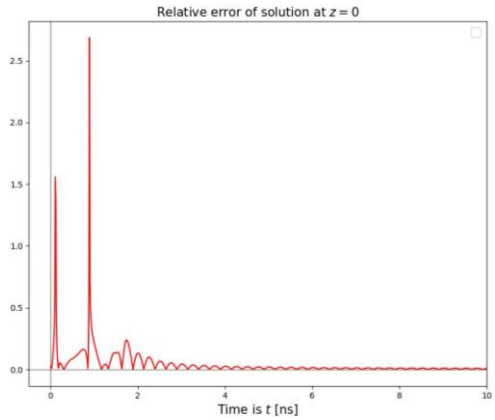

Figure 18
Relative error (in percentage) of the direct problem solution

Conclusions

This study introduces an interdisciplinary approach to subsurface diagnostics by integrating geophysics, mathematical modeling, signal processing, and deep learning. A radargram interpretation method was developed and implemented in the GeoScan32 software. Key processing steps included noise reduction, filtering, layer detection, and estimation of dielectric properties. The Hilbert transform enabled accurate identification of reflection boundaries through energy peaks. Analytical algorithms were used to solve both forward and inverse problems, forming the basis for effective neural network training. The trained model was successfully applied to road pavement diagnostics, demonstrating both scientific validity and practical usefulness. For future research, we propose to incorporate comparative analysis with various machine learning models is recommended to develop higher-performing solutions.

Acknowledgement

This research is funded by the Science Committee of the Ministry of Science and Higher Education of the Republic of Kazakhstan (Grant No. AP19680361).

References

[1] M. Jol Harry, Ground Penetrating Radar Theory and Applications, Theory and Applications, 2009, ISBN 978-044453348-7

[2] E. C. Utsi, Ground Penetrating Radar: Theory and Practice, 2017, ISBN 978-008102216-0, 978-008102217-7

[3] Conyers, Lawrence B. and Dean Goodman, Ground Penetrating Radar: An Introduction for Archaeologists. Walnut Creek, CA.: Altamira Press, 1997

[4] Ground Penetrating Radar, edited by David J. Daniels. London, 2004 ISBN 0-86341-360-9

[5] Cannon J. R., DuChateau P., An inverse problem for an unknown source term in a wave equation, SIAM J. Appl. Math. Vol.43 (1983) 553-564

[6] Symes Rakesh W. W., Uniqueness for an inverse problem for the wave equation, Common. Partial Diff., Eq. 13 (1988) 87-96

[7] Engl H. W., Scherzer O., Yamamoto M., Uniqueness and stable determination of forcing terms in linear partial differential equations with overspecified boundary data, Inverse Probl. Vol. 10 (1994), 1253-1276

[8] Yamamoto M. Stability, reconstruction formula and regularization for an inverse source hyperbolic problem by a control method, Inverse Problems, Vol. 11 (1995), 481-496

[9] Karballaeezadeh, , et al. Smart structural health monitoring of flexible pavements using machine learning methods. Coatings 10.11 (2020): 1100

[10] Romanov V. G. Inverse problems for Maxwell's Equations. Romanov, S.I. Kabanikhin. Utrecht, The Netherlands. 1994. – 249 p.

[11] Kabanikhin, S. I. *Inverse and Ill-Posed Problems* . Siberian Branch of the Russian Academy of Sciences Press. Novosibirsk, 2018, 512 pp.

[12] Chapouly M., Mirrahimi M., Distributed source identification for wave equations: An off-line observer-based approach, Automatic Control, IEEE Trans. 57(8) (2012) 2076-2073

[13] Maarten V de Hoop, Tittelfitz Ju., An inverse source problem for a variable speed wave equation with discrete-in-time sources, Inverse Problems, 31 (7), (2015), 075007

[14] Stolt R. H., Migration by Fourier tranform, Geophysics, Vol. 43(1), (1978), 23-43

[15] Ozdemir C., Demirci F., Yigit E., Yilmaz B., A review on Migration Methods in B-Scan Ground Penetrating Radar Imaging, Mathematical Problems in Engineering, Vol. 2014, Article ID 280738, http://dx.doi.org/10.1155/2014/280738

[16] N. S. Kahil, V. Tempe, A. Yeferni, N. Calon, Z. Benkhelfallah, I. Annag, G. Mbongo, Automatic Analysis of Railway Ground Penetrating Radar: Using Signal Processing and Machine Learning Approaches to Assess Railroad Track Substructure, Transp. Res. Procedia 78 (2023) 594-601, https://doi.org/10.1016/j.trpro.2023.11.848

[17] Nabipour, Narjes, et al. Comparative analysis of machine learning models for prediction of remaining service life of flexible pavement. Mathematics 7.12 (2019): 1198

[18] Rapoport M. B. Computer engineering in field geophysics: Textbook for universities. - M.: Nedra, 1993. - 350 p.

[19] Mukanova B. G., Primary processing of georadar signals by the Hilbert transform Bulletin of the L.N. Gumilev ENU. - 2015

[20] Daubechies I., (2006): Ten Lectures on Wavelets, 9e, SIAM

[21] Mallat S., (2008): A Wavelet Tour of Signal Processing, Academic Press

[22] Donoho DL. De-noising by soft-thresholding, IEEE Trans. Inform.Theory 1995;41(3):612-627

[23] Iskakov K. T., Boranbaev S. A., Uzakkyzy, N. Wavelet processing and filtering of the radargram trace, - Eurasian Journal of Mathematical and Computer Applications. This link is disabled, 2017, 5(4), 43-54

[24] Iskakov K. T., Tokseit D. K., Oralbekova Zh. O., Mirgalikyzy T. Creation and testing of a new mathematical software for processing georadar data, Eurasian Journal of Mathematical and Computer Applications, Vol. 7(4), 2019, DOI: 10.32523/2306-6172-2019-7-4-86-99

[25] Karballaeezadeh, et al. Prediction of remaining service life of pavement using an optimized support vector machine (case study of Semnan–Firuzkuh road). Engineering Applications of Computational Fluid Mechanics 13.1 (2019): 188-198

[26] Azodinia, et al. Service Life Modeling of Pavement with Ensemble Learning. 2025 IEEE 12th International Conference on Computational Cybernetics and Cyber-Medical Systems (ICCC) IEEE, 2025

[27] Mudabir, et al. Modeling Remaining Service Life and Structural Health Monitoring of Roads with Machine Learning and Deep Learning. 2025 IEEE 23rd World Symposium on Applied Machine Intelligence and Informatics (SAMI) IEEE, 2025

[28] Ashrafian, Ali, et al. "Classification-based regression models for prediction of the mechanical properties of roller-compacted concrete pavement." Applied Sciences 10.11 (2020): 3707

[29] Rafiq, Waqas, et al. "Life cycle cost analysis comparison of hot mix asphalt and reclaimed asphalt pavement: A case study." Sustainability 13.8 (2021): 4411

[30] Zhang, Guodao, et al. Reliability assessment of compressive and splitting tensile strength prediction of roller compacted concrete pavement: introducing MARS-GOA-MCS. International Journal of Pavement Engineering 23.14 (2022): 5030-5047